

# A phototropic vine-inspired robot with embedded sensing-actuation loops

Shivani Deglurkar<sup>1\*</sup>, Charles Xiao<sup>1\*</sup>, Luke Gockowski<sup>2</sup>, Megan T. Valentine<sup>1</sup>, and Elliot W. Hawkes<sup>1</sup>

**Abstract**—The fields of soft and bio-inspired robotics promise to imbue synthetic systems with capabilities found in the natural world. However, many of these biological capabilities are yet to be realized. For example, vine tendrils in nature direct growth via local sensing and actuation loops, useful for robustness and parallelization particularly when many tendrils search independently for resources (e.g., light). Yet to date, vine-inspired robots have yet to show such local sensing-actuation loops, and instead rely on centralized frameworks, in which sensors in the tendrils pass information back to a central computer, which in turn sends signals back to the tendrils to command actuation. Here we present a vine-inspired robotic device with material-level sensing and actuation loops embedded in its skin and capable of “growing” and steering toward a light stimulus. We present basic modeling of the concept, design details, and experimental results showing its behavior in response to infrared (IR) light. Our simple device advances the capabilities of bio-inspired robots and lays the foundation for future “growing” robots that could be highly parallelized while seeking stimuli. Potential applications include aiding firefighters in finding fires, in which the robots would seek IR radiation from localized fires in a smoke-filled building as well as solar energy harvesting, in which the robots would follow the sun.

## I. INTRODUCTION

Over the past decades, bio-inspired robotics and then soft robotics have gained interest [1], owing partly to their ability to easily adapt to changing environments without complex mechanisms. However, many intriguing behaviors from the natural world are yet to be realized in these compliant robots.

One particularly compelling example is from the plant kingdom: the local sensing-actuation loops in growing tendrils and roots that enable tropisms, or directed motility along a gradient [2]. Growth is directed by environmental cues, such as sunlight or soil dampness, and sensed by individual vines or roots without any central processing [3]. For root systems, hundreds or even thousands of individual roots can simultaneously steer. Further, if some of the vines or roots are damaged or removed, the others remain fully functional. Various vine- and root-inspired robots have been proposed that extend from their tips to “grow”, but none has demonstrated these local sensing-actuation loops to control growth direction.

This work was supported in part by NSF Grants CMMI-1944816 and EFMA-1935327. The work of C. Xiao was supported by the NSF Graduate Research Fellowship Program (2139319).

<sup>1</sup>Department of Mechanical Engineering, University of California, Santa Barbara, CA 93106.

<sup>2</sup>Accenture Labs, San Francisco, CA 94105

\* Equal contribution. Emails: shivani\_deglurkar@ucsb.edu, charles.xiao@ucsb.edu

This work has been submitted to the IEEE for possible publication. Copyright may be transferred without notice, after which this version may no longer be accessible.

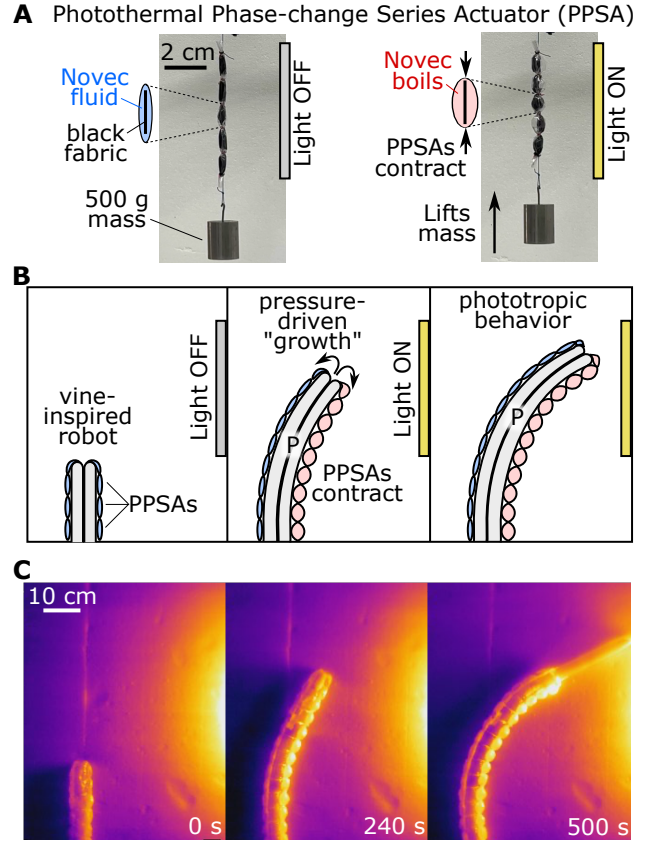


Fig. 1. Overview of phototropic vine-inspired robot concept. **A:** We introduce Photothermal Phase-change Series Actuators (PPSAs), which are filled with low-boiling point Novec 7000. Under light irradiation, the PPSAs absorb light, heat up, inflate with vapor, and contract to lift a mass. **B:** The PPSA can be incorporated onto a vine-inspired robot body. When the robot is inflated to pressure,  $P$ , it “grows” from the tip by unfurling material from inside. At the same time, the PPSAs on the side exposed to light contract, locally sensing and responding to the stimulus. This enables the phototropic behavior. **C:** Realization of the concept: a pneumatic everting robot grows forward and then is deflected toward the right where the light source is located due to the asymmetric expansion of the PPSAs. Image taken with an IR camera, showing PPSAs heating on the side closest to the light. Temperatures range from approximately 20 (yellow) to 40 °C (dark purple). Light flux at the point nearest the source is less than half that of the sun.

One sub-group of this type of robot is the vine-inspired everting robots, or “vine robots,” a class of soft robot made of an inverted, flexible, thin-walled pneumatic tube that everts when pressurized, lengthening from its tip [4], [5], [6], [7], [8], [9]. Because this lengthening involves no relative movement of the body with respect to the environment, the robot can reliably extend through constrained environments, even when the properties of the path and obstacles are unknown.

Current methods for controlling vine robots are central-

ized, relying on sensor data processed by either human operators or an autonomous computer controller to steer towards a target. For human-controlled teleoperation, the operator receives information from the sensors, makes decisions, and sends the appropriate signals to the robot (e.g., [10]). For autonomous control, computer vision can be implemented to parse a scene and direct the robot to a pre-determined target (e.g., [9]). Another method of centralized control scheme uses tropisms, or directed motility along a gradient [2]. Other tip-extending robots have implemented tropisms to sense stimuli such as gravity and moisture, yet also rely on a centralized framework for computing the response to sensors and sending signals to actuators [11].

While such a centralized framework (used in all of these previous works) is useful when a single, low-degree-of-freedom robot is employed, it has limitations when many degrees of freedom need to be controlled (whether in a high-degree-of-freedom single tendril, or many low-degree-of-freedom tendrils). A human operator simply has difficulty controlling dozens of degrees of freedom simultaneously, and a centralized autonomous system grows infeasibly complex (wiring, valving and pumps for actuators, etc.) and increasingly expensive as the number of degrees of freedom in the robot increases.

An alternative is a decentralized approach, with bio-inspired local sensing-actuation loops in each tendril of the robot. This has the potential to enable many active degrees of freedom, but requires that the many sensing-actuation loops are simple and inexpensive. Current steering mechanisms for vine robots, including motorized pull tendons (e.g., [12]), pneumatically-controlled latches (e.g., [9]), and artificial muscles (e.g., [10], [13], [14]), all require electronic sensing, control, and power, limiting their use with many controlled degrees of freedom.

A promising alternative is a “material-level” scheme that leverages the intrinsic materials properties of the soft robot body. The capabilities of a number of functional materials to sense, compute, or actuate in response to external stimuli (such as light, heat, electromagnetic fields, or chemical conditions) have been demonstrated [15], [16]. Among these, light and heat are particularly promising due to the availability of photothermal actuators that can undergo significant changes in properties or volume as a result of light-induced temperature changes [17], [18], [19].

In this work, we present a vine-like robot that uses material-level sensing-actuation loops embedded directly in the skin to achieve phototropism—i.e., directed motion toward a light source (Fig. 1). These many local sensing-actuation loops are achieved using the liquid-gas phase change of a low-boiling-point fluid that is encased in many small, individual pouches along the sides of an everting soft robot body. We call this new actuator a Photothermal Phase-change Series Actuator (PPSA). Due to the non-uniformity of light flux around light sources of finite size, the PPSAs located closest to the light source will actuate first, shortening that portion of the robot facing the light, and steering it toward the light source.

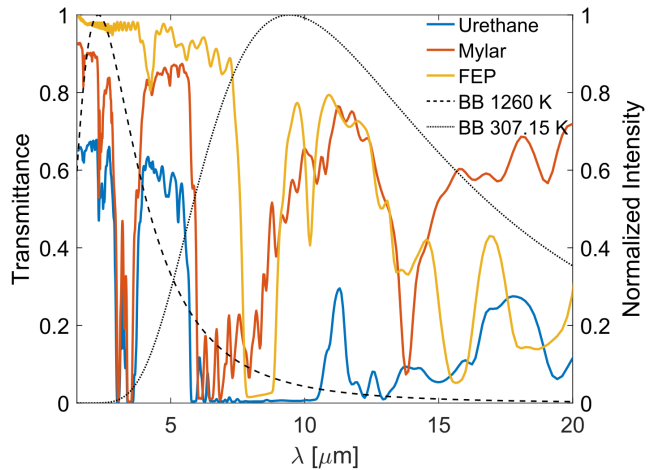


Fig. 2. Transmittance measurements of different materials polymeric materials (solid lines, left axis). The normalized intensity of the blackbody radiation representing the IR lamp (dotted line, right axis) and an object held at the boiling point of Novec 7000 (dashed line, right axis).

The primary contribution of this work is advancing the state of the art in vine- and root-inspired “growing” robots by introducing local sensing-actuation loops. Secondary contributions include the introduction of PPSAs and a method for integration into “vine” robots, as well as a model of the behavior of the resulting devices. We envision potential applications to include aiding firefighters, wherein the robots could seek IR radiation from localized fires in a smoke-filled building as well as solar energy harvesting, wherein the robots could grow toward the sun, like vines in a forest. Below, we first describe the design and fabrication of the device. Then, we characterize the PPSAs and introduce a model that predicts the pose of the robot. Next, we demonstrate a light-seeking vine robot extending in a space with single or multiple IR light sources. We conclude with a discussion of the robot performance and next steps.

## II. DEVICE DESIGN

### A. Robot Design

We have created a robot that steers toward a light source as it extends, or “grows,” based only on the local sensing-actuation loops in the many PPSAs. The robot has a central spine made of a pneumatically pressurized LDPE tube (3.2 cm diameter) that provides structure and enables tip-based growth, flanked by two rows of many individually actuated PPSAs (Fig. 1). The PPSAs are small and flexible for eversion, and described in more detail in the next section. Left-right steering is achieved by differential inflation of the PPSAs. During growth, the PPSAs most exposed to the light source will most absorb light, increase in temperature, and contract. These PPSAs will be the ones on the side of the robot facing the light source and at the position along the robot that is nearest the light. In addition, the inclusion of an internal absorbing sheet (described below) provides a means of “shading” the opposing-side PPSAs, and the pneumatic LDPE spine offers insulation between the two rows of PPSAs—enhancing this differential effect. Thus

contraction occurs preferentially in the PPSAs near the light, resulting in higher curvature in these areas; as in a plant tendril, this drives the tip of the robot toward the light until the robot is pointing directly at the light, and both sides of the robot have equal light exposure.

### B. Photothermal Phase-change Series Actuator (PPSA) Design

We introduce the PPSA, a self-contained, untethered, soft photothermal actuator arranged in series that absorbs light in order to heat a phase-change liquid. The liquid boils, increasing pressure inside the actuator, causing radial swelling and length contraction. The design builds on previous work using electrically heated [20] and laser-heated [19] phase-change liquid in a single flat plastic pouch. In contrast, for the PPSA, the design is a pleated, radially symmetric pouch design similar to the pleated pneumatic artificial muscle (PPAM) [21], [22], which when arranged in series, form a series pneumatic artificial muscle (sPAM) [23]. However, these are actuated by pumping compressed fluid into the actuator, and are thus tethered and not self-contained. As such, sPAMs either each need an independent pressure line and control valve (for high-degree-of-freedom control) or must be tethered together, resulting in constant curvature arcs. In contrast, we isolate the inflation of each PPSA in the series by sealing individually, thereby enabling localized actuator response. We select Novec 7000 as a working fluid due to its low boiling point (i.e., 34 °C at atmospheric pressure), non-toxicity, and compatibility with a broad selection of polymer films, as has been done in previous liquid-to-gas .

Critical to the design of the PPSA is choosing the correct spectral properties to selectively absorb the wavelength of light that a given application requires. For example, we choose to design for an IR light, similar to what would be emitted by a fire, but one could instead design for the spectrum of the sun or a even a specific visible color (making an actuator that only responded to that color or light). To absorb IR light, we considered two paradigms: either using an opaque, absorbing material for the PPSA skin, which requires heat to be conducted to the contained fluid, or using an IR-transparent pouch with an IR-absorber immersed in the working fluid. In the latter case, the skin should be transparent to the primary wavelengths of the source and opaque to the emitted wavelengths, to create a greenhouse effect [24].

To select an appropriate IR-transparent plastic film, we compared the transmittance of urethane, Mylar, and fluorinated ethylene propylene (FEP) films to the estimated blackbody spectrum of our IR light source, as well as the black body spectrum of an object at 307.15 K, which is the boiling point of Novec 7000 (Fig. 2). Unlike urethane, both the Mylar and FEP films show good transmittance to the heat source wavelengths. In practice, however, FEP films were not mechanically robust, suffering from leaks during use that were not observed when using Mylar. Further, Mylar has the lowest gas permeability of the films tested. Therefore, Mylar was the best choice and used throughout the experiments.

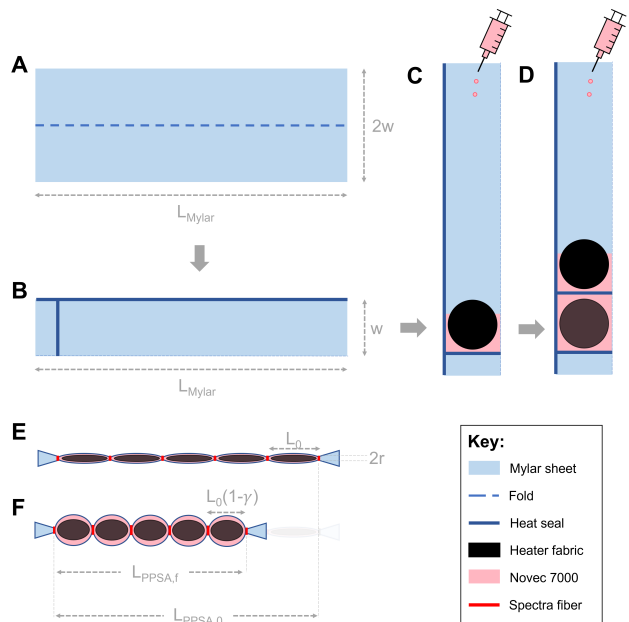


Fig. 3. Schematic of fabrication steps for a 5-pouch PPSA. **A:** Cut Mylar to a 30 cm long ( $L_{\text{Mylar}}$ ) by 9 cm wide ( $W$ ) strip. **B:** Fold in half, length-wise, and heat seal along the length. Create a second heat seal perpendicular to the length and 2.5 cm from the edge to form a 4.5 cm wide chamber. **C:** Place 3.8 cm diameter circle of absorber into sealed pouch; inject 1.5 mL Novec 7000. **D:** Heat seal further down the length, 4.5 cm from previous pouch; repeat for five pouches. **E:** Tie off pouches using spectra fiber. **F:** Inflated pouches show contraction.

However, we note that it is relatively stiff, which causes the actuators to produce less force and strains than expected (see Sec. IV-A.3).

To test the effect of absorber configuration on response time, we measured the time for a single PPSA pouch to transition from fully deflated to fully inflated when fixed to a polystyrene foam block positioned 76 cm away from the quartz heater. Each PPSA pouch (7.0 cm  $\times$  3.7 cm) was heat-sealed with equal volumes of Novec 7000 inside. Four conditions were tested: (A) clear Mylar pouch containing a black nonwoven microfiber fabric sheet (EonTex NW170-PI-20), (B) clear Mylar pouch with the microfiber sheet adhered to the surface using double-sided tape, (C) aluminized Mylar pouch with a microfiber fabric sheet adhered to its surface, (D) aluminized Mylar pouch with the surface coated with matte black spraypaint (Krylon Ultra Flat Camouflage). The response times of conditions A, B, C, and D were 95, 270, 105, and 150 seconds, respectively. The fastest configuration, clear Mylar containing an internal microfiber fabric sheet (condition A), was selected for the design of our PPSA.

### III. FABRICATION

The PPSAs were constructed from a rectangular strip of clear Mylar folded onto itself length-wise, and heat sealed along its length. Then, a perpendicular heat seal created a chamber (Fig. 3A, B). Next, a circle of microfiber fabric sheet was slipped in from the unsealed edge until it reached a heat sealed edge. Thereafter, Novec 7000 was injected into

the chamber, and enclosed with a heat seal further down the pouch long axis from the previous heat seal (Fig. 3C, D). This process was repeated to produce 5 flat pouches in series. Finally, Spectra fiber (*Power Pro 80 lb test*) was tied onto the four seals separating each pouch and at the two ends (Fig. 3E). This changes the geometry from flat pouches to a pleated, radially symmetric pouch. Constraining the actuator geometry in this way has been demonstrated as a method to achieve higher contraction ratios compared to flat pouches [23]. The robot was then assembled as follows. First, multiple sets of the 5-pouch PPSAs were connected in series using zip ties. Next, these sets of PPSAs were adhered to opposing sides of the LDPE spine using double-sided tape. Lastly, the robot body was inverted and pressurized.

#### IV. SEMI-EMPIRICAL MODEL

The goal of the model is to predict the pose of the robot for a given light flux. To do this, we use a semi-empirical model, combining an empirical component and an analytical component. For the empirical component of the model, we use experimental data to determine the relationship between light flux and contraction ratio of the PPSA. For the analytical component of the model, we use a static pose model to relate the contraction ratio of the PPSAs to the pose of the robot at equilibrium.

##### A. Empirical Component: Light Flux to Contraction Ratio

To determine the empirical relationship between flux and contraction ratio, we first measured the flux as a function of distance from the light source (i.e., infrared lamp) and then measured the contraction ratio as a function of distance from the light. By combining the results from these two experiments, we infer the flux-contraction ratio relation.

1) *Flux versus Distance from Light*: To experimentally determine the relationship between flux and distance from the light source, we measured the equilibrium temperature of a plate at varying distances. For the light source, we used an infrared lamp (Infratech W-7512 SS) with an approximate peak emission wavelength of  $2.3\ \mu\text{m}$  (see Fig. 2). For the plate, we used a black-painted aluminum plate ( $\sim 1.6\ \text{cm} \times 1.6\ \text{cm}$ ). At all separation distances, the center of the plate was placed 2 cm above the polystyrene floor, which is at a height that is approximately level with PPSAs on the robot. At each position, we measured and recorded the equilibrium temperature,  $T_{plate}$  with a K-type thermocouple (ThermoWorks K-36X) attached to the back side of the plate. For simplicity, we assumed the plate is a blackbody, which is reasonable since the paint has high emissivity, and used a vertical flat plate convection model (Eq. 9.27 of [24]) to estimate the flux as:  $Q_{light} = \sigma T_{plate}^4 - h(T_{plate} - T_{amb})$ . As expected, the flux nearly obeys the inverse square law (Fig. 4A). Using IR imaging (FLIR E60) we determined the spatial distribution of flux around the lamp (Fig. 4B). We assume isotherms are isofluxes.

We attribute the primary uncertainty of Fig. 4A to the uncertainty of the convection model. Free convection coeffi-

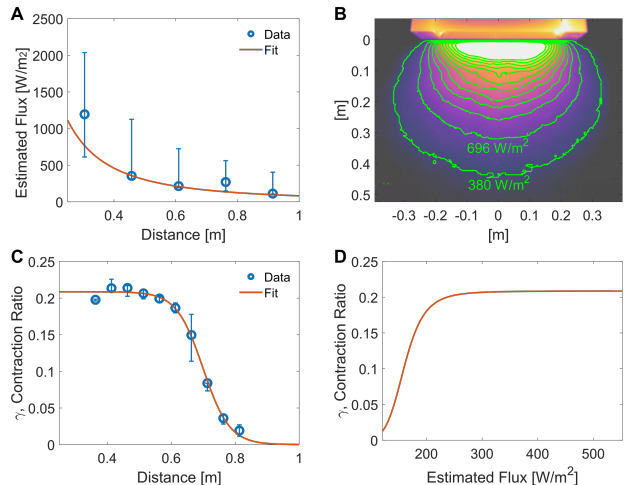


Fig. 4. The empirical component of the model is built from flux versus distance data combined with contraction ratio versus distance data. **A**: First, we measure flux as a function of distance from the light source. The circles are the experimentally measured points and the solid line is an exponential fit to the data. **B**: IR image of the temperature produced by lamp on a polystyrene foam floor. The contours represent isotherms, which we interpret as isoflux lines. **C**: Second, we measure contraction ratio as a function of distance from the light source, for a fixed force level of 5 N. **D**: Finally, we assemble these two relationships to create a representation of the relationship between contraction ratio and flux.

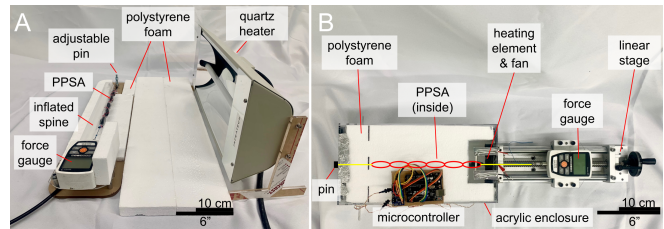


Fig. 5. Images of the testing setups. **A**: Setup for measuring the relationship between flux and the distance from the IR source (Fig. 4). **B**: Temperature-controlled setup for measuring the force-contraction ratio relationship at different temperatures (Fig. 6).

icients,  $h$ , typically varies from 2 to  $25\ \text{W}/\text{m}^2$  (Table 1.1 of [24]).

2) *Contraction Ratio versus Distance from Light*: Next, we measured the contraction ratio at different distances along the centerline of the light source at a predetermined force level. A 5-pouch PPSA was suspended by two pieces of Spectra fiber (*Power Pro 80 lb test*). One end of the fiber was pinned and the other was attached to a force gauge (Mark-10 M3-5) on an adjustable stage (Fig 5A).

The PPSA was backed with a 5 cm diameter LDPE tubing to simulate the heat transfer effects of the central spine. In each test, the system was equilibrated for 12 minutes to reach steady state and the displacement required to produce 5 N of force was measured. This allowed the contraction ratios to be measured as a function of distance (Fig. 4C). Using experimental and theoretical arguments (see Sec. IV-A.3), we fitted a sigmoidal function to the data.

The uncertainty comes from the discrete adjustments of the stage used. The pin was moved between pre-drilled holes on the stage. We used a linear interpolation to find the

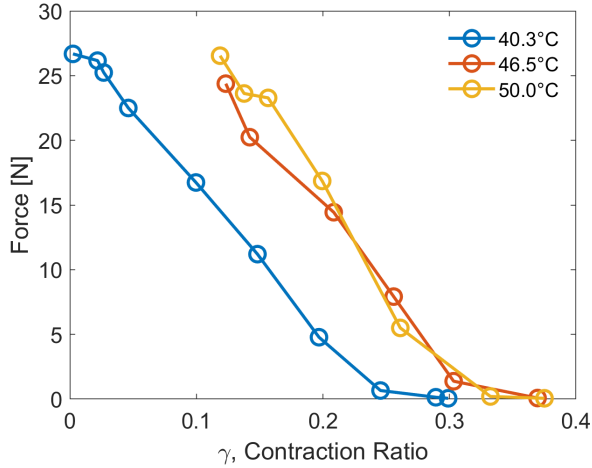


Fig. 6. Force vs. contraction ratios for different temperatures. Moving from the lowest temperature (blue) to the middle temperature (red), the PPSA contracts substantially more at a given force level (e.g., 5 N). However, a further increase in temperature (yellow) does not further increase contraction ratio. This behavior explains the sigmoidal shape in Fig. 4C and D.

contraction ratio that exerts 5 N.

This experiment was designed to ensure that the illumination conditions were similar to those of the previous experiment, allowing us to estimate the relationship between contraction ratio and flux (Fig. 4D). The exponential fit of Fig. 4A was used to convert distance to flux of the fitted relationship in Fig. 4C.

As long as the flux is known (and in the correct flux range, wavelengths, etc.), the relationship in Fig. 4D allows us to predict the contraction of the PPSAs in environments beyond the centerline of Fig. 4B.

3) *Interpretation:* The sigmoidal shapes in Fig. 4C and D can be explained by the relationship between temperature and the shape of the PPSA force-contraction ratio curve (Fig. 6). To measure this, we placed PPSAs inside a temperature-controlled insulated box (Fig. 5B). A linear stage adjusted the contraction ratio and a force gauge measured the forces. We observed that as temperature (and thus internal pressure) increases, the location of the force-contraction ratio curve to the right. Specifically, we observed that at a given force level, the contraction ratio initially increased as the temperature was increased from 40.3°C to 46.5°C. However, as the temperature was further increased to 50.0°C, saturation occurs, and the curves no longer shift to the right. This saturation effect with respect to temperature is reflected in the sigmoidal shapes seen in Fig. 4C and D. At low fluxes (and relatively large distances), the effective temperatures (and pressures) inside the PPSAs are lower; thus, the contraction ratios approach 0. Whereas, at higher fluxes, the effective temperatures and pressures increase, until above a certain threshold value, which we experimentally determined to be  $\sim 250 \text{ W/m}^2$  for our system, increasing the flux does not result in a larger contraction ratio.

We also note that while the previous PPAM and sPAM models [22], [21] qualitatively describe the observed shapes

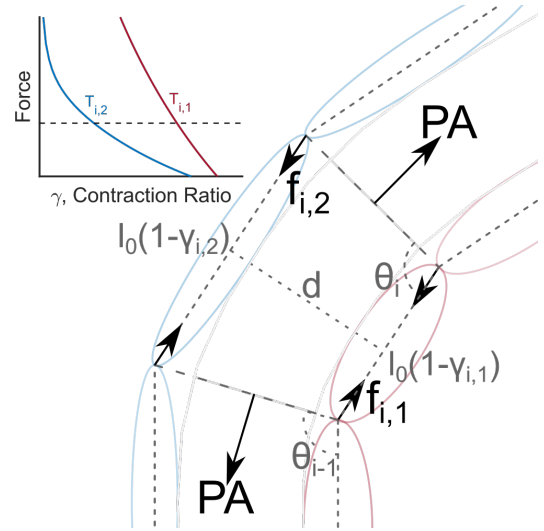


Fig. 7. Detail of the static pose model. The outline of the robot is shown in light gray, the trapezoidal geometry and dimensions are shown in a darker gray, and the forces are shown in black. The higher temperature PPSA, which is closer to the light source, is shown in red (and its force-contraction ratio curve is shown on the inset). Similarly, the lower temperature PPSA is shown in blue. Note that the two PPSAs will have the same force, but different contraction ratios.

in Fig. 6 (i.e., a monotonic decrease in force with increasing contraction ratio), the models predict larger forces at a given contraction ratio and a larger maximum contraction ratio. This is possibly because the models did not consider the effects of materials with non-negligible bending stiffness and internal hysteresis. The multi-layer Mylar film we use is noticeably less supple than the polyethylene of [23], due to the requirement for it to be gas impermeable over long times scales (days). As such, we instead used an empirical relationship for this component of our model.

### B. Analytical Component: Static Pose Model

In this section, we present the analytical component of the model, which predicts the static pose of the robot given the force-contraction ratio relationship of each of the PPSAs along the robot body (determined from the empirical component of the model, given a light flux). The contraction-ratio of each PPSA varies due to temperature differences caused by differences in light flux at each PPSA.

To form this static pose model, we first discretize the vine robot body into a series of  $N$  trapezoidal sections, each consisting of three springs (representative element shown in Fig. 7). The center spring represents the pneumatic axial expansion force, and the two outer springs represent the PPSAs. We assume there are no forces between the trapezoidal sections (i.e., all forces are internal to each section), because we assume the robot is free from external contacts (i.e., horizontal on a frictionless surface).

The force and moment balances within the  $i$ -th section are respectively

$$PA = f_{i,1}(\gamma_{i,1}) + f_{i,2}(\gamma_{i,2}), \quad (1)$$

$$f_{i,1}(\gamma_{i,1}) = f_{i,2}(\gamma_{i,2}). \quad (2)$$

$P$  is the gauge pressure of the pneumatic backbone,  $A$  is the cross-sectional area of the backbone,  $f$  is the force exerted by the PPSA, and  $\gamma$  is contraction ratio of the PPSA. The subscripts 1 and 2 denote which side of the robot the PPSAs are on. For Fig. 7, we chose the 1 side to be the light source side and 2 to be the side away from it. For static balance to occur  $f_{i,1}(\gamma_{i,1}) = f_{i,2}(\gamma_{i,2}) = PA/2$ . The  $i$ -th angle can be determined from the relation

$$l_0(1 - \gamma_{i,1}) + \frac{d}{\tan(\pi - \theta_{i-1})} + \frac{d}{\tan(\pi - \theta_i)} = l_0(1 - \gamma_{i,2}), \quad (3)$$

where  $d$  represents the width spacing between the two PPSAs. For simplicity, we assume this value is constant.

This model shows that even though the contraction ratio and temperature of opposing PPSAs may be different, the force exerted will be the same. This is because the tension in the each of the two PPSAs at a given cross section will be equal and opposite to half of the axial expansion pressure inside the pneumatic backbone, as shown in (1) and (2).

So at equilibrium, the force exerted by each PPSA depends solely on the pressure of the pneumatic backbone and is independent of temperature. However, the exact contraction ratio of a certain PPSA depends on the pneumatic backbone pressure and the temperature of the PPSA.

For example, if the backbone is exerting an expansion force of 10 N, each of the two PPSAs on either side will be applying 5 N, regardless of which one is closer to the light; however, the one that is closer to the light and hotter will have a greater contraction ratio (Fig. 7, Inset).

## V. RESULTS

### A. Verification of Semi-Empirical Model

We tested the semi-empirical model by comparing the predicted shape with the experimental one (Fig. 8). For the test, we used a simple scene and analyzed a section of the robot where the flux varies little in the direction parallel to the source, so that the contraction ratio versus distance data in Fig. 4 is applicable. Additionally, we assume the side away from the light is sufficiently shielded so that the contraction ratio on the more distant side is zero ( $\gamma_{i,2} = 0$ ). The center body was inflated to approximately 12 kPa, so that the required deformation force is 5 N,  $l_0$  is 4.1 cm, and  $d$  is 5.0 cm.

Fig. 8 superimposes the predicted shape, in orange, over the image of the experimental shape. Near the base, there is good agreement, but towards the tip, the model over-predicts the curvature. We attribute this overestimation to the fact that as the robot turns towards the source, the PPSAs on the opposing side begin to receive non-negligible exposure to the source causing them to heat up and contract. This results in less curvature of the robot than is predicted with the assumption of zero contraction ratio for these opposing PPSAs. The heating of the opposing PPSAs near the tip can be seen in the IR image shown in the inset. Note that the undulations of the predicted shape are an artifact of the trapezoid geometry used in the model.

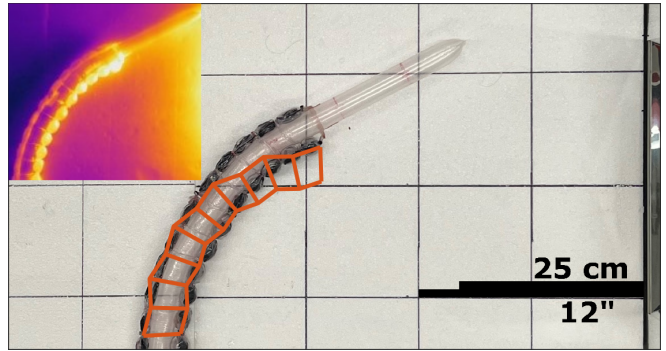


Fig. 8. Model verification on a section of robot. The predicted shape, in orange, is drawn over the image of the experiment. Inset shows the infrared image of the test. The light source is located at the right edge of the figure.

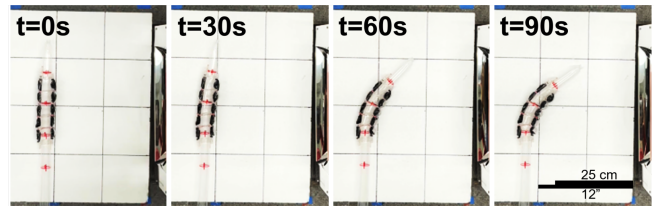


Fig. 9. The robot can steer towards the heat source within 90 s.

### B. Demonstrations

We first test the response speed of the robot in the simple case of being placed next to a light source (at a distance of  $\sim 35$  cm), as shown in Fig. 9. Full turning of the vine robot body by the photothermal PPSAs, each individually responding to the light, occurs in  $\sim 90$  s. We note that we demonstrate the turning process when the robot is already everted. Since the robot is stiffer when there are PPSAs inside the body, a higher actuation force is required, which takes longer to achieve.

Second, we demonstrate the robot growing via internal pressure and steering autonomously with local PPSA-based sensing-actuation loops toward the light source in three different scenarios. The light is relatively low power, with the flux that reaches the robot ranging from approximately 10-15% that of sunlight ( $\sim 1000$  W). Fig. 10A shows the simplest case with a single robot and light source, and shows how the robot tip bends to grow straight towards the light source, as the PPSAs on the lit side of the robot contract. Fig. 10B adds a second robot, showing how these devices can work in parallel. Further, this shows with the right-hand robot that the robot can find the light source even if it is initially growing away from it. Fig. 10C shows another scenario with two robots growing in parallel, this time each seeking a different light source. This divergent behavior is enabled because each robot will respond most strongly to the light source that is closest to it, meaning one can turn toward the left of the picture while the other turns toward the right.

## VI. CONCLUSIONS AND FUTURE WORK

This work demonstrates the design, testing, modeling, and deployment of a phototropic vine-inspired robot capable of

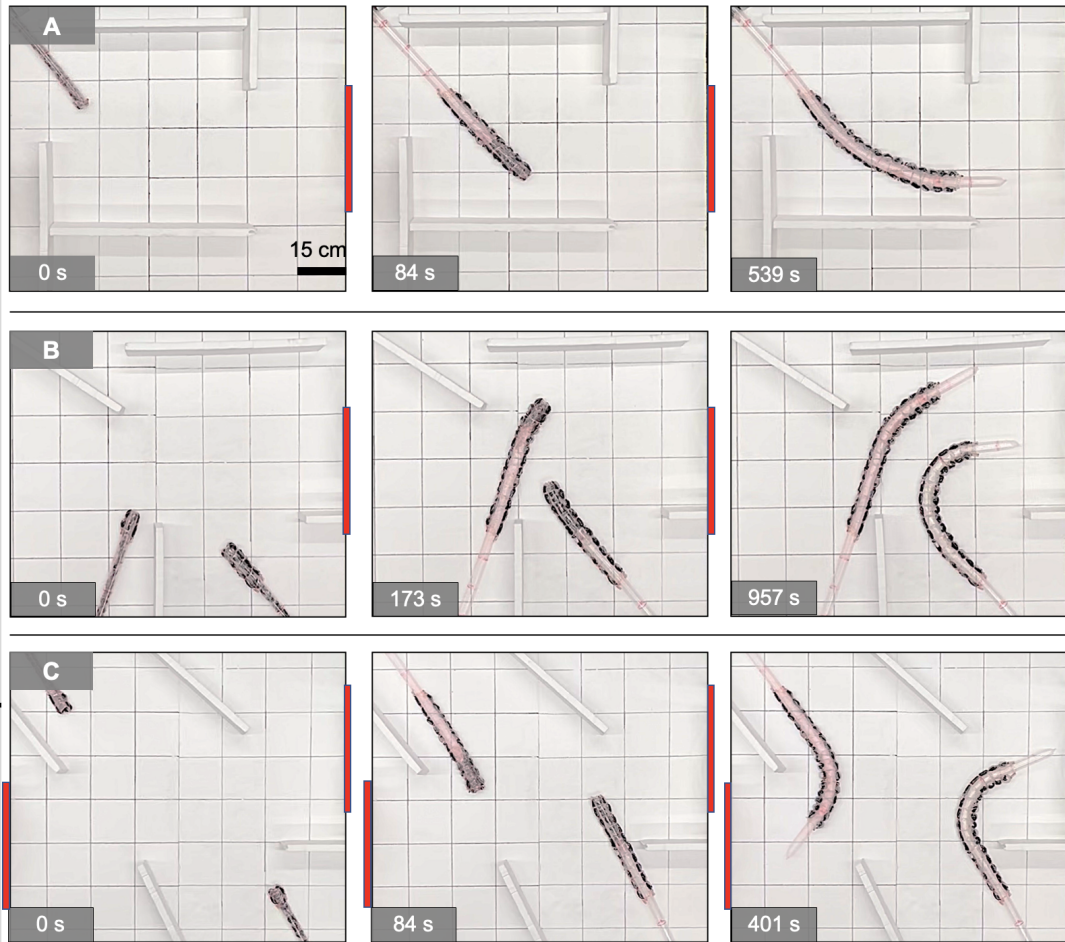


Fig. 10. Demonstrations of thermotropic eversion toward the indicated light source(s) (represented by red boxes) in unknown environments. The PPSAs on opposing sides of the vine robot body actuate asymmetrically under photothermal activation, enabling the robot to bend and grow in a path defined by the styrofoam barriers. **A:** Eversion of one vine robot towards a light source on the right. **B:** Eversion of two vine robots towards the same light source. **C:** Eversion of two vine robots towards two light sources on the left and right.

autonomous motion toward a light. The robot makes use of a central pneumatically-pressurized spine for support and to drive eversion, while embedded sensing-actuation loops in the PPSAs control direction of motion. We presented a semi-empirical model of the robot with sufficient resolution to capture the trends of the robot’s kinematic response to an external light source. This model was validated through experimental analysis of the pose in a simple light field. Demonstrations of the robot showed its ability to use its local sensing and actuation loops to autonomously control its direction of growth and seek a light source. Further demonstrations showed multiple robots exhibiting phototropic steering while seeking the same or different light sources.

In the current iteration with the relatively low-power light, the response of the robot is on the order of minutes. However, for applications with much higher fluxes, this response time would become shorter. For instance, direct sunlight would offer over twice the flux, and cut the response time substantially. And for applications to aid fire-fighting, fluxes over  $100\text{ kW/m}^2$  may be encountered [25] (over a hundred times greater flux than used here). Of course, materials with higher melting temperatures would be required in such cases,

which could lead to other constraints in the design. Another possible variation of the proposed design for the fire-seeking application is to use carbon dioxide as the working fluid (instead of Novec 7000). Carbon dioxide absorbs strongly at the wavelengths emitted by fire, meaning the robot could selectively sense fire rather than other hot objects [26].

Overall, this demonstration represents a significant step forward in our understanding of how to incorporate material-level sensing and actuation loops into vine-inspired robots and soft robots generally.

## VII. ACKNOWLEDGEMENTS

We thank Professor Michael Gordon’s research group for performing the transmittance measurements in Fig. 2, and David Haggerty for his editing help.

## REFERENCES

- [1] E. W. Hawkes, C. Majidi, and M. T. Tolley, “Hard questions for soft robotics,” *Science robotics*, vol. 6, no. 53, p. eabg6049, 2021.
- [2] B. Mazzolai, “Growth and tropism,” *Living Machines: A Handbook of Research in Biomimetics and Biohybrid Systems*; Prescott, TJ, Lepora, N., Verschure, PFMJ, Eds, pp. 99–104, 2018.
- [3] B. Forde and H. Lorenzo, “The nutritional control of root development,” *Plant and soil*, vol. 232, no. 1, pp. 51–68, 2001.

- [4] D. Mishima, T. Aoki, and S. Hirose, "Development of pneumatically controlled expandable arm for search in the environment with tight access," in *Field and Service Robotics*. Springer, 2003, pp. 509–518.
- [5] T. Viebach, F. Pauker, G. Buchmann, G. Weighlofer, and R. Pauker, "Everting sleeve system," Patent, July 5, 2006, european Patent 1676598A2.
- [6] H. Tsukagoshi, N. Arai, I. Kiryu, and A. Kitagawa, "Smooth creeping actuator by tip growth movement aiming for search and rescue operation," in *2011 IEEE International Conference on Robotics and Automation*. IEEE, 2011, pp. 1720–1725.
- [7] —, "Tip growing actuator with the hose-like structure aiming for inspection on narrow terrain," *International Journal of Automation Technology*, vol. 5, no. 4, pp. 516–522, 2011.
- [8] A. Sadeghi, A. Tonazzini, L. Popova, and B. Mazzolai, "Robotic mechanism for soil penetration inspired by plant root," in *2013 IEEE International Conference on Robotics and Automation*. IEEE, 2013, pp. 3457–3462.
- [9] E. W. Hawkes, L. H. Blumenschein, J. D. Greer, and A. M. Okamura, "A soft robot that navigates its environment through growth," *Science Robotics*, vol. 2, no. 8, p. eaan3028, 2017.
- [10] M. M. Coad, L. H. Blumenschein, S. Cutler, J. A. R. Zepeda, N. D. Naclerio, H. El-Hussieny, U. Mehmood, J. Ryu, E. W. Hawkes, and A. M. Okamura, "Vine robots: Design, teleoperation, and deployment for navigation and exploration," in preparation.
- [11] A. Sadeghi, A. Mondini, E. Del Dottore, V. Mattoli, L. Beccai, S. Taccola, C. Lucarotti, M. Totaro, and B. Mazzolai, "A plant-inspired robot with soft differential bending capabilities," *Bioinspiration & biomimetics*, vol. 12, no. 1, p. 015001, 2016.
- [12] S. Wang, R. Zhang, D. A. Haggerty, N. D. Naclerio, and E. W. Hawkes, "A dexterous tip-extending robot with variable-length shape-locking," in *2020 IEEE International Conference on Robotics and Automation (ICRA)*. IEEE, 2020, pp. 9035–9041.
- [13] J. D. Greer, T. K. Morimoto, A. M. Okamura, and E. W. Hawkes, "A soft, steerable continuum robot that grows via tip extension," *Soft robotics*, 2018.
- [14] M. Selvaggio, L. Ramirez, N. D. Naclerio, B. Siciliano, and E. W. Hawkes, "An obstacle-interaction planning method for navigation of actuated vine robots," in *2020 IEEE International Conference on Robotics and Automation (ICRA)*. IEEE, 2020, pp. 3227–3233.
- [15] Z. Shen, F. Chen, X. Zhu, K.-T. Yong, and G. Gu, "Stimuli-responsive functional materials for soft robotics," *Journal of Materials Chemistry B*, vol. 8, no. 39, pp. 8972–8991, 2020.
- [16] Y. Zhao, M. Hua, Y. Yan, S. Wu, Y. Alsaïd, and X. He, "Stimuli-responsive polymers for soft robotics," *Annual Review of Control, Robotics, and Autonomous Systems*, vol. 5, 2021.
- [17] J. Han, W. Jiang, D. Niu, Y. Li, Y. Zhang, B. Lei, H. Liu, Y. Shi, B. Chen, L. Yin, *et al.*, "Untethered soft actuators by liquid–vapor phase transition: remote and programmable actuation," *Advanced Intelligent Systems*, vol. 1, no. 8, p. 1900109, 2019.
- [18] S. M. Mirvakili, A. Leroy, D. Sim, and E. N. Wang, "Solar-driven soft robots," *Advanced Science*, vol. 8, no. 8, p. 2004235, 2021.
- [19] T. Hiraki, K. Nakahara, K. Narumi, R. Niiyama, N. Kida, N. Takamura, H. Okamoto, and Y. Kawahara, "Laser pouch motors: Selective and wireless activation of soft actuators by laser-powered liquid-to-gas phase change," *IEEE Robotics and Automation Letters*, vol. 5, no. 3, pp. 4180–4187, 2020.
- [20] K. Nakahara, K. Narumi, R. Niiyama, and Y. Kawahara, "Electric phase-change actuator with inkjet printed flexible circuit for printable and integrated robot prototyping," in *2017 IEEE International Conference on Robotics and Automation (ICRA)*. IEEE, 2017, pp. 1856–1863.
- [21] F. Daerden and D. Lefeber, "The concept and design of pleated pneumatic artificial muscles," *International Journal of Fluid Power*, vol. 2, no. 3, pp. 41–50, 2001.
- [22] F. Daerden, "Conception and realization of pleated pneumatic artificial muscles and their use as compliant actuation elements," *Vrije Universiteit Brussel*, p. 176, 1999.
- [23] J. D. Greer, T. K. Morimoto, A. M. Okamura, and E. W. Hawkes, "Series pneumatic artificial muscles (spams) and application to a soft continuum robot," in *2017 IEEE International Conference on Robotics and Automation (ICRA)*. IEEE, 2017, pp. 5503–5510.
- [24] T. L. Bergman, F. P. Incropera, D. P. DeWitt, and A. S. Lavine, *Fundamentals of heat and mass transfer*. John Wiley & Sons, 2011.
- [25] "2 - fires and thermal environments," in *Thermal Protective Clothing for Firefighters*, ser. Woodhead Publishing Series in Textiles, G. Song, S. Mandal, and R. M. Rossi, Eds. Woodhead Publishing, 2017, pp. 5–15.
- [26] R. Linares, G. Vergara, R. Gutiérrez, C. Fernández, V. Villamayor, L. Gómez, M. González-Camino, and A. Baldasano, "Gas and flame detection and identification using uncooled mwir imaging sensors," in *Thermosense: Thermal Infrared Applications XXXVII*, vol. 9485. SPIE, 2015, pp. 385–390.